Fabric-enriched Modeling of Anisotropic Healing induced by Diffusion in Granular Salt

Zhu, C. and Arson, C.

Geosystems group, School of Civil and Environmental Engineering,
Georgia Institute of Technology, Atlanta, Georgia, USA.

ABSTRACT: This study aims to model anisotropic damage (i.e. increase of porosity and loss of stiffness) and healing (i.e. recovery of stiffness) in salt rock subject to microcrack initiation, propagation, and rebonding. We introduce enriched fabric tensors in a Continuum Damage Mechanics model to link micro-crack evolution with macroscopic deformation rates. We carry out creep tests on granular salt assemblies to infer the form of fabric descriptors. We use moments of probability of fabric descriptors to find relationships between microstructural and phenomenological variables. Creep processes in salt include glide, cross-slip, diffusion, and dynamic recrystallization. We assume that healing is predominantly governed by diffusive mass transfer. We model the corresponding crack cusp propagation on grain faces by means of a two-dimensional diffusion equation. We calibrate this grain-scale healing model against experimental measures of crack cusp propagation distance. We simulate the opening, closure and rebonding of three orthogonal families of micro-cracks during a compression-tension loading cycle. Multi-scale model predictions illustrate the evolution of stiffness, deformation, and crack geometry during the anisotropic damage and healing process, and highlight the increased healing efficiency with time. We expect that the proposed modeling approach will provide more precise and reliable performance assessments on geological storage facilities in salt rock.

1. INTRODUCTION

Because of its low permeability, water solubility and self-healing properties, salt rock is a favorable host rock for the geological storage of nuclear waste, oil and natural gas, compressed air (CAES), and hydrogen. Salt properties depend on the state of damage and recovery of the rock, which undergoes temperature and stress cycles around storage facilities. In order to understand and predict the microscopic mechanisms at the origin of damage and healing, we propose to model anisotropic thermo-mechanical damage and healing processes by means of alternative fabric descriptors.

Thermo-mechanical damage and healing models of salt rock proposed in continuum mechanics rely on the concept of dilatancy boundary [1]. Anisotropic healing models based on Continuum Damage Mechanics (CDM) usually resort to the concept of "net damage", which allows modeling stiffness degradation (damage) and recovery (healing). These theoretical frameworks are purely hypothetical and do not allow the prediction of all coupled processes that occur in actual rock materials. Rock damage models that distinguish closure and rebonding conveniently model all dissipation processes with rate-dependent evolution laws, which avoids

implementing threshold-based yield functions in numerical codes. Unfortunately, those models do not properly represent the brittle behavior resulting from rate-independent crack opening and closure. In such models, healing is defined as a particular form of crack closure detected by an increment in wave velocity, rather than crack rebonding.

In our previous models [2, 3], we accounted for mechanical anisotropy induced by crack opening and closure, and we assumed that diffusive mass transfer (DMT) leading to crack rebonding produced isotropic healing at the scale of the Representative Elementary Volume (REV). In this work, we model the two-dimensional diffusion of ions through crack or grain faces. In our model, diffusion triggers only when cracks are closed and stresses applied at the faces are compressive, which yields different intensities of healing in the different directions of space. The fabric-enriched model proposed in this paper thus accounts for the mechanical anisotropy induced by healing over time, and not only for the mechanical anisotropy induced by damage. Since the healing process requires external stimulations, we qualify this type of self-healing process as passive, similar to the close-then-heal scheme [4].

In order to describe the evolution of the crack pattern during damage propagation and healing, we analyzed microscope images of granular salt at various stages of creep tests. We used these tests as an analog of salt rock creep tests, in which grain boundaries represent cracks. Our experimental study was intended to highlight microstructure descriptors that can be used to define damage and healing variables. In section 2, we explain how we selected the two fabric descriptors that we introduced in our formulation. We present the multi-scale theoretical framework coupling crack opening, closure, and healing in Section 3. In Section 4, we simulate a load cycle to show the influence of anisotropic damage and healing on mechanical behavior and microstructure evolution.

2. FABRIC DESCRIPTORS

Observing fabric evolution under complex paths of stress, moisture and temperature remains a challenge to experimentalists. In this work, we used table salt grain assemblies, which possess the same halite content and crystallographic structure as salt rock. We carried out continuous observations of fabric changes in salt grains subjected to a creep load [3]. The sample was confined in an acrylic tube, and loaded axially by a spring (Fig. 1). We compressed the spring to different extents in order to apply specific pressures ranging from 0.1 MPa to 0.2 MPa. We observed that the spring length was almost constant throughout the test, which allowed us to assume that we were applying a constant stress. As shown in Figure 1, we ensured a constant humidity environment (humidity level = 75%) by injecting air through oversaturating salt water, as explained in [5].
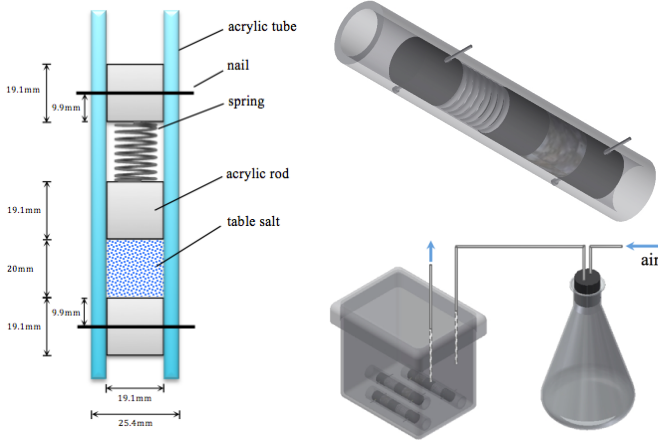

Fig. 1. Injection of moist air into the container through saturated salt water.

In order to avoid taking out the sample and extracting thin sections, we observed compressed salt grains through the tube at regular time intervals. Transparent and cubic table salt grains easily reflect light, which impairs image quality. We used *ImageJ* [6] for image processing. We approximated the shape of voids as

ellipses, and proposed to model salt fabric by means of the void area (A_v) and the projection of ellipses major semi-axes in three principal directions of space (noted as crack length r_i) [3]. The area followed a power law distribution as

$$p_A(A_v) = a \cdot A_v^t, \tag{1}$$

in which a and t are constants, with values obtained from the fitting of microscopic data.

The crack length followed a lognormal distribution as

$$p_i(r_i) = \frac{1}{\sqrt{2\pi}r_i s_i} e^{-\frac{(lnr_i - m_i)^2}{2s_i^2}}, \tag{2}$$

in which s_i is the standard deviation and m_i is the mean value.

In recent developments, we added inclusion particles to track grain movement in a fixed region and introduced new plugins in *ImageJ* for better image analysis results [7]. On-going research aims to improve the choice of fabric descriptors to capture microstructure changes during the different creep deformation regimes.

3. THERMO-MECHANICAL MODEL

We proposed a multi-scale modeling framework that coupled anisotropic healing with CDM, in order to capture the effect of crack opening, closure, and healing on deformation and stiffness variations. Table 1 presents the outline of the theoretical framework for anisotropic damage and healing.

3.1. Continuum Damage Model

For a typical loading-unloading cycle, we decomposed the total strain into three components (Fig. 2). $\boldsymbol{\varepsilon}^{el}$ denotes the purely elastic deformation and is recoverable upon unloading. ε^d is the damage deformation induced by crack propagation and has two components: ε^{ed} is the damage-induced elastic deformation, ε^{id} the irreversible deformation as a result of residual crack openings. We defined the additional compressive stress required to compensate ε^{id} as the residual stress:

$$\boldsymbol{\sigma}_R = -\boldsymbol{D}(\boldsymbol{\Omega}):\boldsymbol{\varepsilon}^{id}, \tag{3}$$

in which $\boldsymbol{D}$ is the stiffness tensor and $\boldsymbol{\Omega}$ is the damage variable.

The solid skeleton free energy consists of the purely thermo-elastic deformation energy (ψ_s^{ET}) and the potential energy of crack faces ($\psi_s^{\Omega T}$). Thermodynamic conjugation relationships give the stress and the damage driving force [8]. Through a dimensional analysis, we showed that the quadratic term in temperature $\frac{\tau^2}{2\tau_0}\frac{\partial C(\boldsymbol{\Omega})}{\partial \boldsymbol{\Omega}}$ can be neglected in the expression of the damage driving force [2]. We further simplified the active damage driving force ($\boldsymbol{Y}_d$) as a function of total strain only. To capture the hardening phenomenon, which accounts for

the release of energy needed for growth of micro-cracks, we expressed the damage criterion (f_d) in the form of a

results in a change of stiffness ($\boldsymbol{D}^*(\boldsymbol{\Omega})$) as well as heat capacity ($\boldsymbol{C}^*(\boldsymbol{\Omega})$).

Table 1. Outline of thermo-mechanical anisotropic damage and healing model

Postulates	
Free Energy for Crack Opening (Ψ_S)	$\psi_s = \psi_s^{ET} + \psi_s^{\Omega T} = \left[\frac{1}{2}\boldsymbol{\varepsilon}^{el}:\boldsymbol{D_0}:\boldsymbol{\varepsilon}^{el} - \frac{C_0\tau^2}{2\tau_0} - \tau\boldsymbol{K_0}:\boldsymbol{\varepsilon}^{el}\right] + \left[\frac{1}{2}\boldsymbol{\varepsilon}^d:\boldsymbol{D}(\boldsymbol{\Omega}):\boldsymbol{\varepsilon}^d - \frac{C(\Omega)\tau^2}{2\tau_0} - \tau\boldsymbol{K}(\boldsymbol{\Omega}):\boldsymbol{\varepsilon}^d\right]$ $\frac{1}{2}\boldsymbol{\varepsilon}^d:\boldsymbol{D}(\boldsymbol{\Omega}):\boldsymbol{\varepsilon}^d = \frac{1}{2}\lambda\left(tr\boldsymbol{\varepsilon}^d\right)^2 + \mu tr\left(\boldsymbol{\varepsilon}^d \cdot \boldsymbol{\varepsilon}^d\right) + \alpha tr\boldsymbol{\varepsilon}^d tr\left(\boldsymbol{\varepsilon}^d \cdot \boldsymbol{\Omega}\right) + 2\beta tr\left(\boldsymbol{\varepsilon}^d \cdot \boldsymbol{\varepsilon}^d \cdot \boldsymbol{\Omega}\right)$
Free Energy for Crack Closure (Ψ_S)	$\psi_s = \left[\frac{1}{2}\boldsymbol{\varepsilon}^{el}:\boldsymbol{D_0}:\boldsymbol{\varepsilon}^{el} - \frac{C_0\tau^2}{2\tau_0} - \tau\boldsymbol{K_0}:\boldsymbol{\varepsilon}^{el}\right] + \left[\frac{1}{2}\boldsymbol{\varepsilon}^d:\boldsymbol{D}^*(\boldsymbol{\Omega}):\boldsymbol{\varepsilon}^d - \frac{C^*(\Omega)\tau^2}{2\tau_0} - \tau\boldsymbol{K}^*(\boldsymbol{\Omega}):\boldsymbol{\varepsilon}^d\right]$ $\boldsymbol{D}^*(\boldsymbol{\Omega}) = \boldsymbol{D}(\boldsymbol{\Omega}) + \eta\sum_{i=1}^3 H\left(-tr(\boldsymbol{P_i}:\boldsymbol{\varepsilon})\right)\boldsymbol{P_i}:\left(\boldsymbol{D_0} - \boldsymbol{D}(\boldsymbol{\Omega})\right):\boldsymbol{P_i},\ 0 < \eta \leq 1$ $\boldsymbol{K}^*(\boldsymbol{\Omega}) = \boldsymbol{K}(\boldsymbol{\Omega}) + \eta\sum_{i=1}^3 H\left(-tr(\boldsymbol{P_i}:\boldsymbol{\varepsilon})\right)\boldsymbol{P_i}:\left(\boldsymbol{K_0} - \boldsymbol{K}(\boldsymbol{\Omega})\right):\boldsymbol{P_i},\ 0 < \eta \leq 1$ $\boldsymbol{C}^*(\boldsymbol{\Omega}) = \boldsymbol{C}(\boldsymbol{\Omega}) + \eta\sum_{i=1}^3 H\left(-tr(\boldsymbol{P_i}:\boldsymbol{\varepsilon})\right)\boldsymbol{P_i}:\left[\left(C_0 - C(\Omega)\right)\boldsymbol{\delta}\otimes\boldsymbol{\delta}\right]:\boldsymbol{P_i},\ 0 < \eta \leq 1$
Free Energy for Crack Rebonding (Ψ_S)	Damage $\boldsymbol{\Omega}$ is replaced by net damage $\boldsymbol{A}$ in the free energy for crack closure $\boldsymbol{A} = \boldsymbol{\Omega} - \boldsymbol{H}$
Damage Criterion (f_d)	$f_d(\boldsymbol{Y_d}, \boldsymbol{\Omega}) = \sqrt{\frac{1}{2}\boldsymbol{Y_d}:\boldsymbol{Y_d}} - \{a_0 + a_1[H(-tr(\boldsymbol{\varepsilon}))\Omega_1 + H(tr(\boldsymbol{\varepsilon}))\Omega_2 + H(tr(\boldsymbol{\varepsilon}))\Omega_3]\}$
Strain Decomposition	$\boldsymbol{\varepsilon} = \boldsymbol{\varepsilon}^E + \boldsymbol{\varepsilon}^{id} = \boldsymbol{\varepsilon}^{el} + \boldsymbol{\varepsilon}^d = \boldsymbol{\varepsilon}^{el} + \boldsymbol{\varepsilon}^{ed} + \boldsymbol{\varepsilon}^{id}$
2D Diffusion Equation for Crack Rebonding at the Grain Scale	$D_x\frac{\partial^2 U}{\partial^2 x} + D_y\frac{\partial^2 U}{\partial^2 y} = \frac{\partial U}{\partial t},\ H_i = H(\sigma_i)(1 - \bar{U})$ $x = \left[\frac{DCV_\Omega(\gamma_{SL}+\gamma_{LV})}{\pi RT}\frac{\delta}{a}\frac{4cos\frac{\theta}{2}}{\alpha^3}t\right]^{0.25}$
Conjugation relationships	
Stress ($\boldsymbol{\sigma}$)	$\boldsymbol{\sigma} = \frac{\partial\psi_S}{\partial\boldsymbol{\varepsilon}^{el}} = \boldsymbol{D_0}:\boldsymbol{\varepsilon}^{el} - \tau\boldsymbol{K_0}$
Damage Driving Force (Y_d)	$\boldsymbol{Y} = -\frac{\partial\psi_S}{\partial\boldsymbol{\Omega}} = -\left[\boldsymbol{D}(\boldsymbol{\Omega}):\boldsymbol{\varepsilon}^d\right]:\frac{\partial\boldsymbol{\varepsilon}^d}{\partial\boldsymbol{\Omega}} - \frac{1}{2}\boldsymbol{\varepsilon}^d:\frac{\partial\boldsymbol{D}(\boldsymbol{\Omega})}{\partial\boldsymbol{\Omega}}:\boldsymbol{\varepsilon}^d + \frac{\tau^2}{2\tau_0}\frac{\partial C(\Omega)}{\partial\boldsymbol{\Omega}} + \tau\boldsymbol{K}(\boldsymbol{\Omega}):\frac{\partial\boldsymbol{\varepsilon}^d}{\partial\boldsymbol{\Omega}} + \tau\frac{\partial\boldsymbol{K}(\boldsymbol{\Omega})}{\partial\boldsymbol{\Omega}}:\boldsymbol{\varepsilon}^d$ $\boldsymbol{Y_d} = -(\alpha + 2\beta)\boldsymbol{\varepsilon}\cdot\boldsymbol{\varepsilon}$

α,β	=	mechanical damage parameters	a_0	=	initial damage threshold
λ,μ	=	Lamé coefficients	a_1	=	damage hardening parameter
τ_0	=	initial temperature	g	=	toughness parameter
$\boldsymbol{D}$	=	damaged stiffness tensor	k	=	bulk modulus
α_T	=	thermal expansion coefficient	$\boldsymbol{K}$	=	$k\alpha_T$ "diagonal tensor"
$\boldsymbol{D}^*$	=	effective stiffness tensor after "partial recovery"	C	=	damaged heat capacity
$\boldsymbol{K}^*$	=	effective diagonal tensor after "partial recovery"	A	=	TM damage parameter
$\boldsymbol{C}^*$	=	effective heat capacity after "partial recovery"	η	=	degree of maximum stiffness recovery
$\boldsymbol{P_i}$	=	4th order project tensor for the projection in crack planes normal to direction i	$\boldsymbol{\delta}$	=	second order identity tensor

norm minus the damage threshold, in which we accounted for the recovery of compression strength by crack closure (Table 1). Note that for simplicity, we chose to use a damage criterion which is independent of temperature variation.

Following a classical CDM assumption [9], we used an associative damage flow rule (i.e., f_d is the damage potential):

$$d\boldsymbol{\Omega} = d\lambda_d\frac{\partial f_d(\boldsymbol{Y_d},\boldsymbol{\Omega})}{\partial\boldsymbol{Y_d}} = \frac{\left[\frac{\boldsymbol{Y_d}}{\sqrt{2\boldsymbol{Y_d}:\boldsymbol{Y_d}}}\right]:d\boldsymbol{Y_d}}{(C_1\boldsymbol{\delta}):\left[\frac{\boldsymbol{Y_d}}{\sqrt{2\boldsymbol{Y_d}:\boldsymbol{Y_d}}}\right]}:\left[\frac{\boldsymbol{Y_d}}{\sqrt{2\boldsymbol{Y_d}:\boldsymbol{Y_d}}}\right]. \qquad (4)$$

We distinguished closed cracks from bonded cracks. We adopted the concept of unilateral effect to account for the recovery of material compressive strength as a result of closure of tensile cracks. Following Chaboche's approach [10], we introduced a Heaviside function in the expression of stiffness, in order to distinguish tension and compression behaviors. Crack closure increases the number of inter-granular contacts in the REV, which
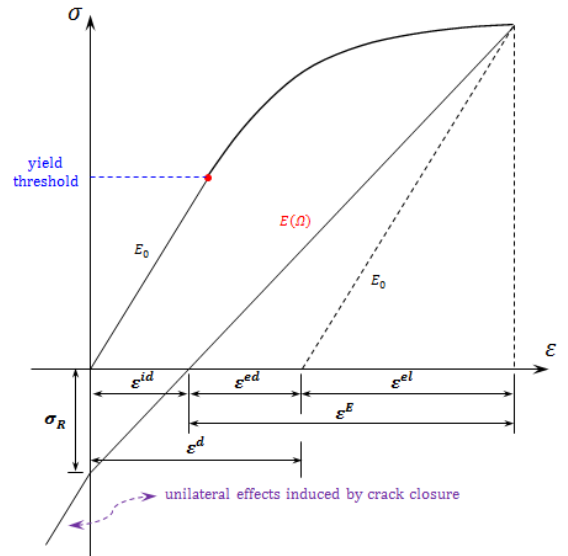

Fig. 2. Decomposition of deformation (soil mechanics sign convention: compression counted positive).

3.2. 2D Diffusion Controlled Healing

We use the microphysical model based on single crack healing experiments conducted by Houben et al. [11] to predict the crack cusp migration distance over time as

$$x = [\frac{DCV_{\Omega}(\gamma_{SL}+\gamma_{LV})}{\pi RT}\frac{\delta}{a}\frac{4cos\frac{\theta}{2}}{\alpha^3}t]^{0.25}, \qquad (5)$$

in which D is the diffusion coefficient, C is the solubility, δ is the fluid film thickness, a is a characteristic length scale, $\alpha = \tan(\frac{\theta}{2})$ is the orientation the crack face (in reference to the loading axis), V_{Ω} is the molecular volume of the solid, γ_{SL} is the solid-liquid interfacial energy, γ_{LV} is the liquid-vapor interfacial energy, R is the gas constant, T is the absolute temperature.

The intensity of damage U varies over the distance x ("lag") that separates the crack cusp and the point at which the crack is fully rebonded (Fig. 3). During the healing process, tubular and porous structures emerging in that lag area induce a partial mechanical recovery. These structures will gradually disappear over time [11].
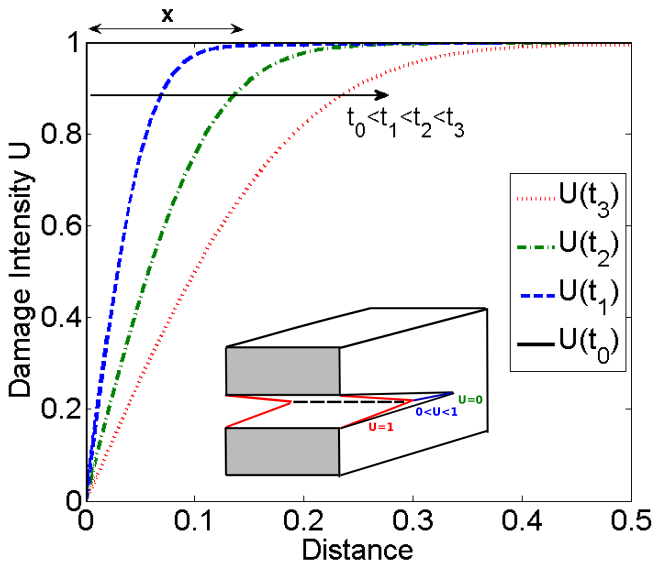
Fig. 3. Schematic model of healing propagation front in a crack (crack cusp migration). Damage intensity U varies from 0 (bonded crack faces similar to an intact material with no crack) to 1 (closed but not bonded faces).

We assume that healing starts at the circumference of crack planes. The crack cusp migrates towards the center of the crack region, according to a two-dimension diffusion process, which is expressed as

$$D_x\frac{\partial^2 U}{\partial^2 x} + D_y\frac{\partial^2 U}{\partial^2 y} = \frac{\partial U}{\partial t}, \qquad (6)$$

in which $U(x,y,t)$ is the damage intensity depending on position and time. D_x and D_y are the diffusion coefficients along x- and y- directions, respectively.

Diffusion in x and y directions affects crack planes perpendicular to the z-direction, and therefore, the z-

component of the damage tensor. Figure 4 shows the variations of damage intensity $U = \Omega z$ within a (x, y) crack plane. The lag distance is indicated by a solid line, over which the damage intensity varies from 0 (at the circumference) and 0 (towards the center of the grain). The mean value of the damage intensity $\bar{U}(t)$ is

$$\int_0^{l_y}\int_0^{l_x} U(x,y,t)dxdy = \bar{U}(t) \cdot A, \qquad (7)$$

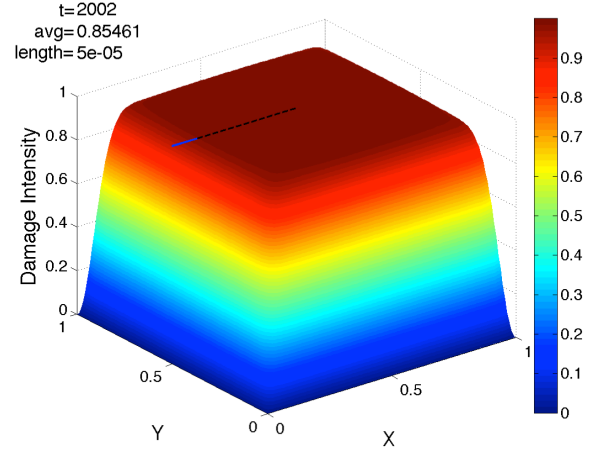in which $A = l_x l_y$ is the crack face area ($A = 1$ for the normalized crack area).

Fig. 4. Distribution of damage intensity during the healing process within one planar crack. The evolution of the lag distance is governed by a 2D diffusion model.

We define the net damage tensor (**A**) as the difference between the damage tensor (**Ω**) and the healing tensor (**H**) as

$$A_i = \Omega_i - H_i = \Omega_i - H(\sigma_i)(1-\bar{U}), \qquad (8)$$

in which $H(\sigma_i)$ is the Heaviside function depending on the stress sign. In our model, we assume that healing takes place in damage directions in which cracks faces are closed and subjected to local compressive stresses (which are known to enhance healing)

High temperature is not a necessary condition for healing to occur. In the presence of brine, thin adsorbed water films between crack faces will assist in accelerating the diffusion process. But higher temperature will provide more efficient healing [3].

3.3. Micro-Macro Relationships

We gather anisotropic micro-cracks into three families of oblate spheroids oriented according to the principal directions of damage (Fig. 5). Therefore, the damage variable is similar to a crack density tensor [12]. The geometry of spheroids is characterized by the crack aperture λ and the crack radius r. We establish the link between fabric changes and phenomenological variables as follows (Fig. 6):

- During elastic loading or unloading, only crack aperture varies

- When damage occurs, crack length increases.
- Healing only occurs when the local stress on the crack face is compressive. During healing, the crack length decreases whereas the aperture remains constant.
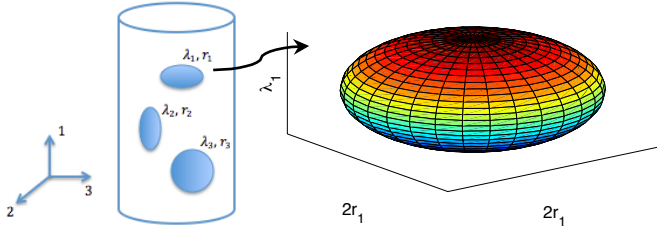

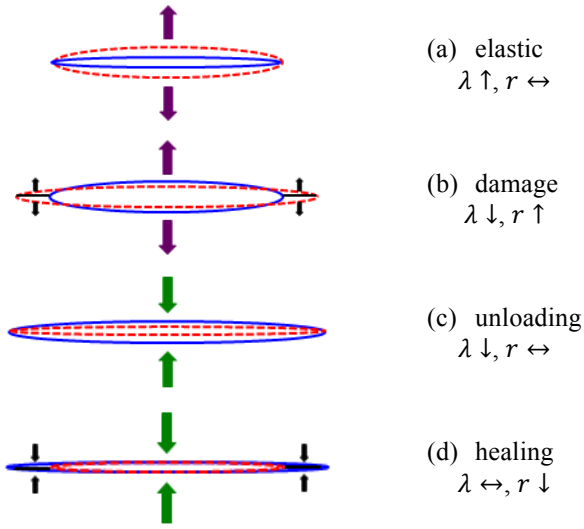Fig. 5. Representation of micro-cracks by three equivalent spheroidal cavities in the REV.

Fig. 6. Geometric evolution of a microcrack projected in a plane perpendicular to the loading direction. Solid lines indicate the original crack geometry and dashed lines indicate the deformed shape.

Note that in our framework, crack radius affects damage and non-elastic deformation, and crack aperture affects elastic and non-elastic deformation.

2D microscopic observations allow us to capture the projected areas of two families of micro-cracks only (Fig. 7). We approximate area projections of these cracks as ellipses.

Assuming that the principal directions of stress and net damage are parallel, we relate net damage eigenvalues (A) to the means of the crack length components (r_j) as presented in Table 2. In the probability density functions, we update only the means m_i and use a constant value for the standard deviations (which are insensitive to variations of pressure and temperature conditions according to our previous studies [3]). The computational steps to update the probability density

function of r_j from the macroscopic strain $\Delta\varepsilon$ are given in Figure 8.

In our framework, grains are incompressible. Therefore, the change of porosity in the REV is equal to the volume change. We could not capture the three-dimensional volume change of the void through 2D microscopic observation. We calculated 3D porosity from 2D porosity by using a linear interpolation. The upper bound of porosity was obtained in the initial state, when salt particles are assembled in a loose packing before creep test starts. We obtained the lower bound of porosity at maximum packing, by making some assumptions on the arrangement of grains (more details are available in [3]). Given the range of possible values for porosity, we were able to update the probability density function of the void area (Fig. 8).
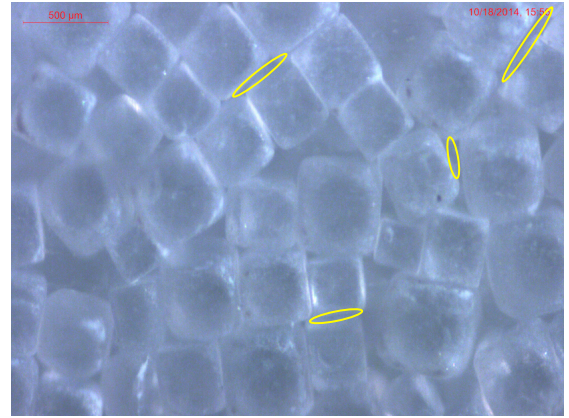

Fig. 7. Microscopic observation of table salt grains during the creep tests. For illustration, we drew a few ellipses that show how to approximate void projections into elliptical shapes.

Using the strain decomposition, we expressed the stress tensor as

$$\boldsymbol{\sigma} = \boldsymbol{D}(\boldsymbol{\Omega}):\boldsymbol{\varepsilon}^E - \tau\boldsymbol{K}(\boldsymbol{\Omega}). \qquad (9)$$

The stress rate under isothermal conditions is

$$
\begin{aligned}
d\boldsymbol{\sigma} &= \boldsymbol{D}(\boldsymbol{\Omega}):d\boldsymbol{\varepsilon} + \frac{\partial \boldsymbol{D}(\boldsymbol{\Omega})}{\partial \boldsymbol{\Omega}}:\boldsymbol{\varepsilon}:d\boldsymbol{\Omega} - d\big[\boldsymbol{D}(\boldsymbol{\Omega}):\boldsymbol{\varepsilon}^{id}\big] \\
&= \boldsymbol{D}(\boldsymbol{\Omega}):d\boldsymbol{\varepsilon} + \frac{\partial \boldsymbol{D}(\boldsymbol{\Omega})}{\partial \boldsymbol{\Omega}}:\boldsymbol{\varepsilon}:d\boldsymbol{\Omega} + d\boldsymbol{\sigma}_R
\end{aligned}
\qquad (10)
$$

Assuming that micro-cracks do not interact, we treat the solid matrix surrounding each crack as an isotropic linear elastic material. We adopt the theory of fracture mechanics [13] to compute the micro-crack opening vector of an ellipsoidal micro-crack propagating in mode I. The micro-crack displacement in the direction perpendicular to the micro-crack axis is (Fig. 9):

$$u_y(R,\theta) = \frac{K_I}{2\mu}\sqrt{\frac{R}{2\pi}}\sin\left(\frac{\theta}{2}\right)[\kappa + 1 - 2\cos^2\left(\frac{\theta}{2}\right)], \qquad (11)$$

in which u_y is half of the crack aperture at location (R,θ), K_I is the stress intensity factor in mode I at the crack tip ($R = 0$), and μ is the shear modulus of the

linear elastic bulk material. κ depends on the bulk Poisson's ratio ν. K_I relates to the microscopic residual stress that applies to the micro-crack faces: $K_I = \sigma_r\sqrt{\pi r}$. When $\theta = \pi$, and $R = r$ in Eq. (11), in which r is half of the crack length, the half aperture $0.5\lambda_a$ defined above is equal to the displacement u_y, which gives:

$$\frac{1}{2}\lambda_a = \frac{\kappa + 1}{2\sqrt{2}\mu}r\sigma_r \tag{12}$$

With the void area $A_v = 0.5\pi\lambda_a r$, we can obtain the macroscopic residual stress for N_v micro-cracks (Table 2).

Table 2 summarizes the relations between fabric descriptors and macroscopic variables. Figure 8 describes the computational method used to update macroscopic variables from the knowledge of microscopic descriptors.
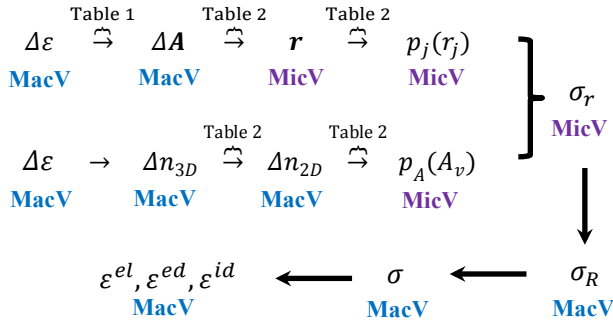
Fig. 8. Computation method to update macroscopic variables (MacV) from microscopic variables (MicV).
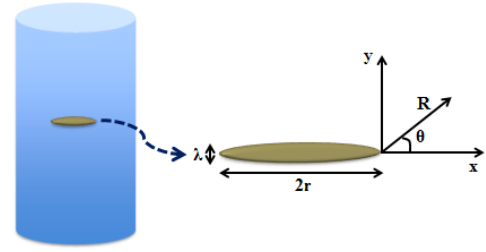

Fig. 9. Schematic representation of a micro-crack subjected to a residual stress within the REV.

4. NUMERICAL SIMULATION

4.1. Calibration of the 2D Diffusion Model

We calibrated the diffusion-controlled healing model against the experimental data provided in Table 3. The first eight values are taken from [11, 14, 15]. α is the slope of the crack wall, which has the same order of magnitude as those values adopted in [11]. d is the diffusion distance, which is equal to the half of a typical crack size [11]. D_x and D_y are parameters to be calibrated for the healing model. Since the structure of salt crystals is symmetric, we assume: $D_x = D_y$, which implies that healing occurs at the same rate along the x- and y- directions of each face. The lag $x(t)$ in Eq. (5) is the distance between a point at the circumference of the initial crack plane and a point at the circumference of the current crack plane, after healing has started. We considered that the position of the current crack circumference was at the point at which $U = 1 \pm 5\%$ (Fig. 3). We calibrated the diffusion coefficient in order

Table 2. Correlations between microscopic and macroscopic variables

Relation between fabric descriptors and phenomenological variables	
R and A	$A = \sum_{j=1}^{3} A_j e_j \otimes e_j$, $A_1 = N_v \frac{\overline{r_1^3}}{V_{REV}}$, $A_2 = N_v \frac{\overline{r_2^3}}{V_{REV}}$, $A_3 = N_v \frac{\overline{r_3^3}}{V_{REV}}$ $\overline{r_j} = \int r_j p_j(r_j)dr_j$
n_{3D} and A_v	$\frac{n_{3D} - n_{3D,lower}}{n_{3D,upper} - n_{3D,lower}} = \frac{n_{2D} - n_{2D,lower}}{n_{2D,upper} - n_{2D,lower}}$ $n_{2D,lower} = \frac{A_{v,lower}}{A_{REV}} = \frac{\pi r^2}{l^2}$, $n_{3D,lower} = \frac{V_{v,lower}}{V_{REV}} = \frac{\frac{4}{3}\pi r^3}{l^3}$ $n_{2D,upper} = \frac{A_{v,upper}}{A_T}$, $n_{3D,upper} = \frac{V_{v,upper}}{V_T}$, $V_{v,upper} = V_T - V_s = A_{tube} \cdot L_{upper} - \frac{m_s}{\rho_s}$ $\overline{n_{2D}} = \int \frac{A_v}{A_{REV}} p_A(A_v)dA$
Relation between fabric descriptor and residual stress	
σ_R and R, A_v	$\sigma_R = N_v\sigma_r = N_v \frac{2\sqrt{2}}{\pi} \frac{\mu}{\kappa + 1} \frac{A_v}{r^2}$

$\overline{r_j}$	$=$	Mean value of crack length	A_j	$=$	Net damage in principal direction j
$n_{2D,lower}$	$=$	Lower bound of 2D porosity	V_{REV}	$=$	Volume of REV
$n_{3D,lower}$	$=$	Lower bound of 3D porosity	σ_R	$=$	Macroscopic residual stress for N_v cracks
$n_{2D,upper}$	$=$	Upper bound of 2D porosity	σ_r	$=$	Macroscopic residual stress for single crack
$n_{3D,upper}$	$=$	Upper bound of 3D porosity	A_T	$=$	Longitudinal cross-sectional area of the sample cylinder
V_s	$=$	Volume of the salt solid	V_T	$=$	Total volume of the sample cylinder
ρ_s	$=$	Density of the salt solid	A_v	$=$	Void area
m_s	$=$	Mass of the salt solid	A_{tube}	$=$	Inner cross-sectional area of tube

to minimize the difference between the numerical and experimental values of x after 20,000 seconds of healing. Despite some deviations induced by the technique we used to update the position of the crack circumference, the time evolution of the lag predicted with the calibrated model follows the trends observed experimentally (Fig. 10).

Table 3. Parameters adopted for the diffusion-controlled healing model (Eqs. (5) and (6))

R (JK^{-1}mol^{-1})	T (K)	D (m^{2}s^{-1})	C (-)
8.314	296	1.3e-9	0.1675
γ_{SL} (Jm^{-2})	γ_{LV} (Jm^{-2})	Ω (m^{3}mol^{-1})	δ/a (-)
0.129	0.064	2.7e-5	9e-13
α	d (m)	D_x (m^{2}s^{-1})	D_y (m^{2}s^{-1})
2.5e-3	1e-4	9e-7	9e-7
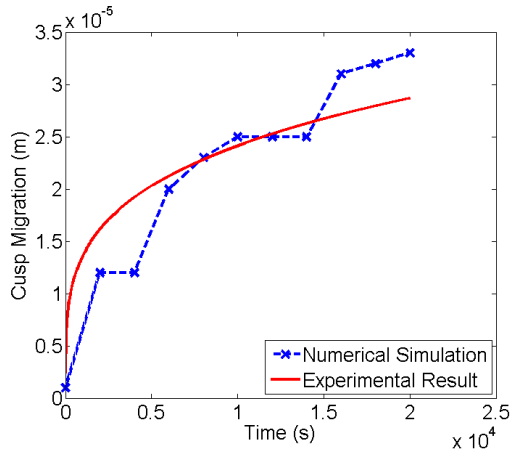
Fig. 10. Calibration of the two-dimensional diffusion-controlled healing model against the experimental result. (Due to the technique we used to update the position of the crack circumference, the numerical curve has a step-wise shape).

4.2. Numerical Analysis at the REV scale

We simulated a strain-controlled one-dimensional loading test in MATLAB. In order to generate anisotropic damage in the specimen, we simulated a compression-tension loading cycle, in stress conditions similar to those encountered in CAES or gas storage sites [16]. The loading cycle consisted of uniaxial compression, followed by compression unloading, uniaxial tension, tension unloading, time-dependent healing, and reloading in tension. We assumed that the tension and compression loads were applied instantaneously, and that the healing phase was the only time-dependent load step. We assumed that the initial porosity of the sample was due to pre-existing micro-cracks with various orientations (i.e. damage was non-zero in the initial state before loading: $\Omega_1 = 0.01, \Omega_2 = \Omega_3 = 0.02$). We assumed that these micro-cracks were filled with saturated brine, which triggered DMT and consequent healing. Table 4 provides the model parameters used in the simulations, after [3, 17].

To facilitate the calculation of macro-micro relationships, we made a few simplifying assumptions:
- During elastic compression, cracks perpendicular to the loading axis close, whereas cracks parallel to the axis keep the same shape.
- When the strain increment is tensile, only the cracks perpendicular to the loading axis change shape.

Table 4. Model parameters used for the strain-controlled uniaxial test (compression counted positive)

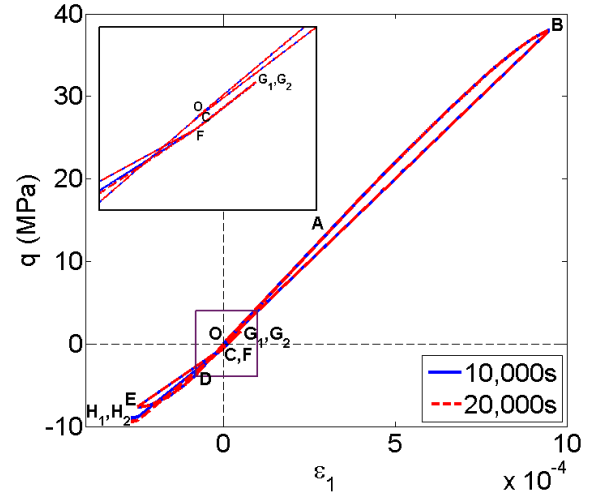| λ (Pa)	μ (Pa)	α (Pa)	β (Pa)
2.63e10	1.75e10	1.9e9	-2.04e10
g (Pa)	C_0 (Pa)	C_1 (Pa)	α_T (K^{-1})
1.1e8	200	1e5	-1e-5
U_0 (-)	l (m)	e_0 (-)	t (-)
1	1e-4	0.008	-1.2
$n_{2D.lower}$ (-)	$n_{2D.upper}$ (-)	$n_{3D.lower}$ (-)	$n_{3D.upper}$ (-)
0.03	0.165	0.004	0.321
R_{min} (m)	R_{max} (m)	A_{min} (m^2)	A_{max} (m^2)
1e-6	1e-4	1e-14	1e-12

Fig. 11. Stress-strain curve simulated for the compression-tension cycle (The magnified portion shows the details of the unilateral effects).

We performed numerical simulations at room temperature (296K) for two different diffusion periods: 10,000s and 20,000s. Contrary to our previous study [3], healing is fast even at room temperature because we assumed here that the inter-granular space was filled with aqueous films. Figure 11 presents the overall stress-strain response of the sample. Under compression (in direction 1), the sample behaves elastically before reaching the damage threshold (OA). Damage starts to accumulate afterwards, causing significant stiffness degradation (AB). Compression unloading is elastic (i.e. cracks parallel to direction 1 do not propagate), therefore the response of the material on portion BC is linear elastic, with a stress-strain slope that is smaller than during the loading phase OA, because of the accumulation of damage on portion AB.
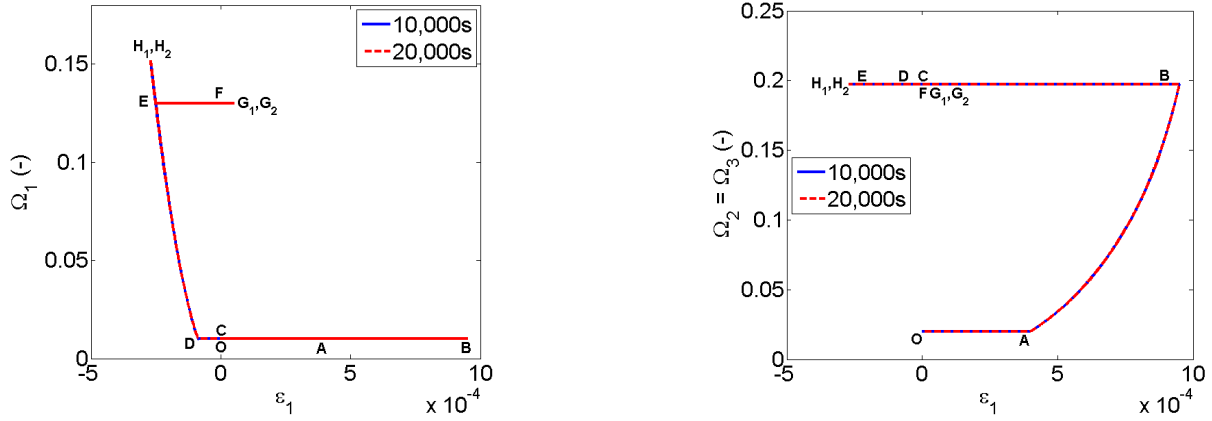
Fig. 12. Evolution of the damage variable. Cracks perpendicular to the loading axis (left) and parallel to the loading axis (right).
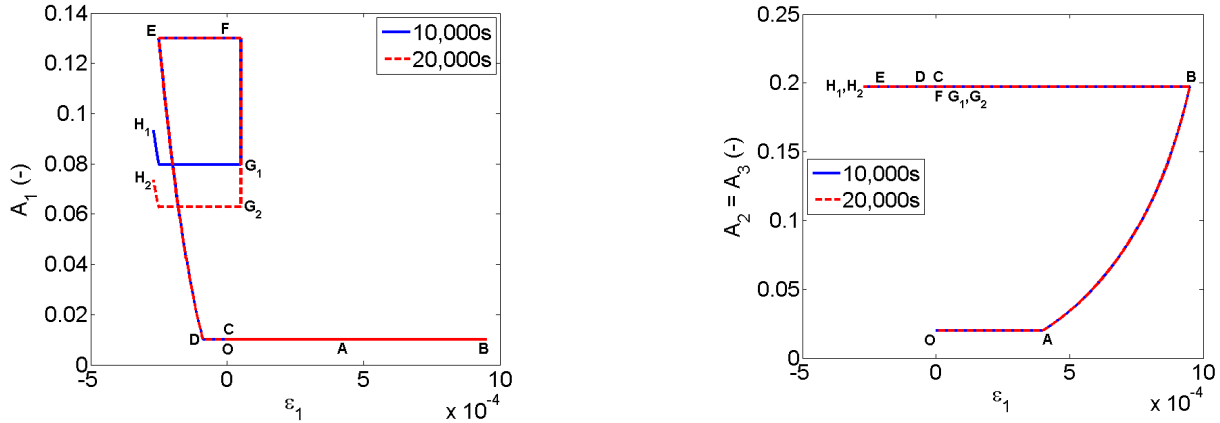

Fig. 13. Evolution of net damage. Cracks perpendicular to the loading axis (left) and parallel to the loading axis (right).

Point C lies slightly below the origin, which indicates the presence of residual stress after unloading. At C, the axial deformation is zero: we assume that cracks are closed at that point. Portion CD (in tension) illustrates the recovery of compression strength after crack closure (i.e., the slope of the stress-strain curve is the same as portion OA). In this particular simulation, a smaller value was assumed for compression strength than for tension strength – as expected for rocks. At D, damage starts to propagate in tension, up to point E. EF shows the elastic tension unloading that follows. At F, tension cracks (perpendicular to direction 1) are closed, and compression cracks (parallel to direction 1) start to re-open. The stress-strain plot of compression reloading (FG) is parallel to that of compression unloading (BC). We simulated the healing phase (constant stress, varying time) under the compression stress at point G. Portions GH_1 and GH_2 show the response of the material when the material is reloaded in tension (for two different healing periods). The slopes of GH_1 and GH_2 are steeper than that of DE and less steep than that of OA, which indicates partial mechanical recovery. As expected, higher recovery is achieved for longer healing periods.

Figure 12 illustrates the evolution of the damage variable. As expected, micro-cracks perpendicular to direction 1 (loading axis) do not propagate during the compression phase (OC) nor during the elastic phase under tension (CD). Damage in direction 1 propagates during the non-elastic tension phases (DE, GH) and remains constant during the unloading and healing phases (EFG). Damage in directions 2 and 3 (micro-cracks parallel to the axis of the loading) increase during non-elastic compression (AB) and remain constant during compression unloading and tension loading (BH). The evolution of net damage in Figure 13 is the same as that of damage except for portion GH, after healing has occurred. Cracks parallel to the loading axis do not heal under compression, therefore damage and net damage in directions 2 and 3 are equal. Cracks perpendicular to the loading axis heal at constant controlled deformation, which explains the drop of net damage after point G. On portion GH, net damage in direction 1 remains constant until the recovered tensile strength is exceeded. Longer healing periods lead to a larger decrease of net damage.

Figures 14 and 15 show the evolutions of the fabric descriptors introduced in the model. By construction of the model, the evolution of crack length mirrors that of net damage. The mean of void areas is proportional to the porosity of the sample, which varies like the volumetric deformation in our model. The mean void area of micro-cracks perpendicular to direction 1 decreases first because of the compression of cracks during the elastic state, remains constant after damage occurs (because we assume that cracks parallel to the loading axis dominate deformation during compression), and increases again when tension is applied. On the

other hand, the surface area of compression cracks varies only during compression phases. Healing under compression leads to a drop in the mean void area of cracks perpendicular to the loading axis. Since cracks parallel to the loading axis do not rebond, their mean area does not change during the healing phase GH.

Figure 16 illustrates the distribution of the damage intensity within a crack face of normalized area. We verify that longer healing periods provide longer lags and therefore lower damage intensity along the grain

also matches with the decrease in net damage variable (shown in Fig. 13).

5. CONCLUSION

We improved our previous continuum mechanics model of crack opening, closure and rebonding to account for the anisotropy of healing – and not only the anisotropy of damage. We modeled crack rebonding as a process governed by the 2D diffusion of ions through crack or grain faces. Diffusion triggers only when cracks are
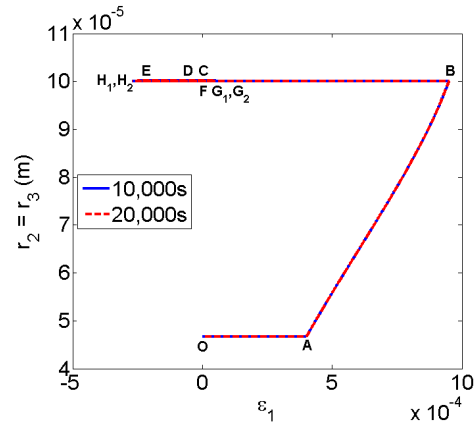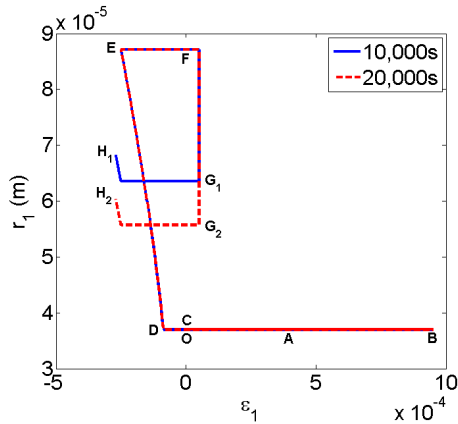

Fig. 14. Evolution of crack length. Cracks parallel to the loading axis (left) and parallel to the loading axis (right).
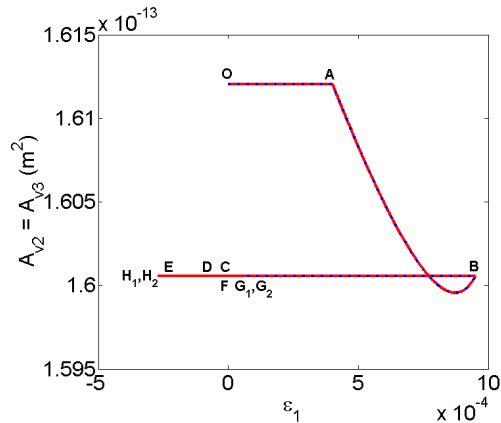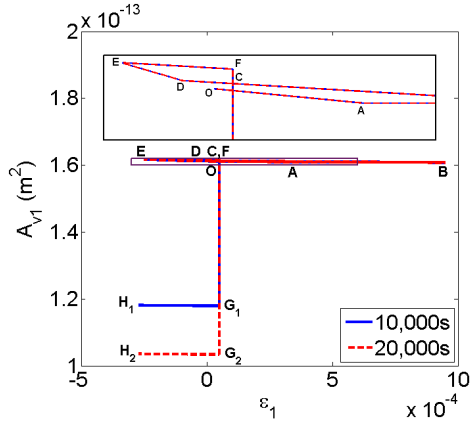

Fig. 15. Evolution of mean crack area. Cracks parallel to the loading axis (left) and parallel to the loading axis (right).
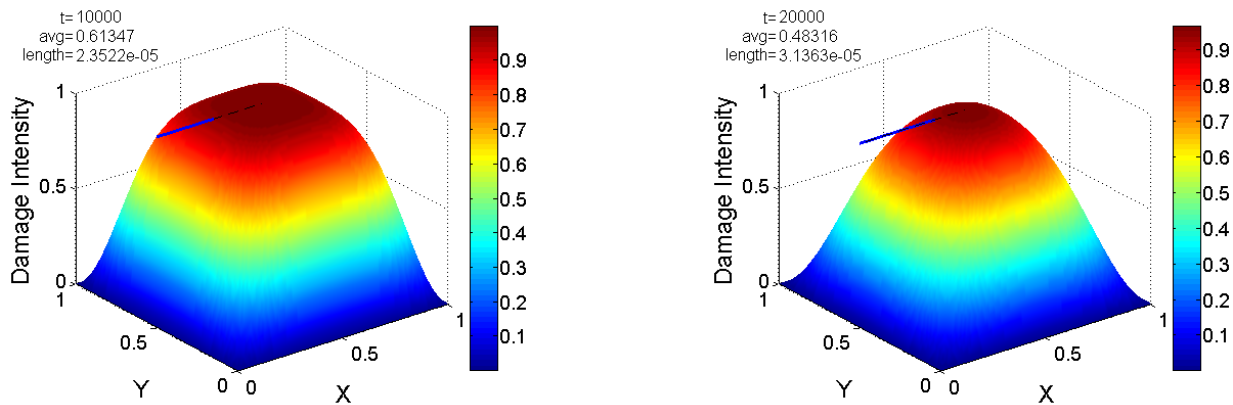

Fig. 16. Damage intensity after two different healing periods (grain scale).

radial direction. We also check that the lags shown in Figure 16 are in agreement with the drop in crack lengths calculated during the healing phase (Fig. 14). The average damage intensity value (shown in Fig. 16)

closed and when stresses applied at the faces are compressive, which yields different intensities of healing in the different directions of space. The free energy is a polynomial comprising a thermo elastic component and

a purely damaged energy component. The damage tensor is similar to a crack density tensor. We defined damage and healing variables from probability density functions of fabric descriptors obtained by image analysis during creep tests performed on granular salt. We provided a computational method to couple phenomenological variables to these descriptors, in order to characterize the rearrangement and rebonding of salt grains.

We programmed the proposed model at the integration point in MATLAB. The stress path is a complete compression-tension cycle that mimics the gas pressurization and depressurization processes in typical CAES conditions. The model captures anisotropic damage and healing processes, illustrates the evolution of both phenomenological variables and fabric descriptors, and highlights the influence of the healing period on stiffness recovery and healing efficiency. We calibrated the diffusion-controlled healing model formulated at the grain scale against published experimental results. Complementary experimental studies of fabric evolution under various temperature or humidity conditions will be conducted in an environmental chamber in order to verify the assumptions made in the model. We expect that our modeling approach will advance the fundamental understanding of damage and healing in salt at different scales, and enable better predictions of the long-term behavior of underground geological storage facilities.

ACKNOWLEDGEMENT

REFERENCES

1. Hou, Z.M. 2003. Mechanical and hydraulic behavior of rock slat in the excavation disturbed zone around underground facilities. *International Journal of Rock Mechanics and Mining Sciences*. 40(5): 725-738.

2. Zhu, C. and C. Arson. 2014. A thermo-mechanical damage model for rock stiffness during anisotropic crack opening and closure. *Acta Geotechnica*. 9(5): 847-867.

3. Zhu, C. and C. Arson. 2014. A model of damage and healing coupling halite thermo-mechanical behavior to microstructure evolution. *Geotechnical and Geological Engineering, Special Issue: Thermo-hydro-mechanical behavior of soils and energy geostructures*. DOI: 10.1007/s10706-014-9797-9.

4. Li, G. and N. Uppu. 2010. Shape memory polymer based self-healing syntactic foam: 3-D confined thermo-mechanical characterization. *Composites Science and Technology*. 70(9): 1419–1427.

5. Wexler, A. and S. Hasegawa. 1954. Relative humidity temperature relationships of some saturated salt solutions in the temperature range 0^0C to 50^0C. *Journal of Research of the National Bureau of Standards*. 53(1): 19-26.

6. Zhu, C., S.H. Jeong, M. Dutta, and C. Arson. 2015. Image Processing of Fabric Evolution in Salt Granular Assemblies subject to Diffusive Mass Transfer. *Mechanical Behavior of Salt VIII, Rapid City, South Dakota, 26-28 May 2015* (in press).

7. Abramoff, M.D., P.J. Magalhaes, and S.J. Ram. 2004. Image processing with *ImageJ*. *Biophotonics international*. 11(7): 36–42.

8. Collins, I. and G. Houlsby. 1997. Application of thermomechanical principles to the modelling of geotechnical materials. *Proceedings of the Royal Society of London Series A: Mathematical, Physical and Engineering Sciences*. 453(1964): 1975–2001.

9. Dragon, A., D. Halm, and T. D´esoyer. 2000. Anisotropic damage in quasi-brittle solids: modelling, computational issues and applications. *Comput Methods Appl Mech Eng* 183(3): 331–352.

10. Chaboche, J.L. 1992. Damage induced anisotropy: on the difficulties associated with the active/passive unilateral condition. *Int. J. Damage. Mech*. 1(2): 148–171.

11. Houben, M.E., A.ten Hove, C.J. Peach, and C.J. Spiers. 2013. Crack healing in rocksalt via diffusion in adsorbed aqueous films: microphysical modeling versus experiments. *Physics and Chemistry of the Earth, parts A/B/C*. 64: 95-104.

12. Kachanov, M. 1992. Effective elastic properties of cracked solids: critical review of some basic concepts. *Appl. Mech. Rev*. 45(8): 304–335.

13. Anderson, T. 2005. *Fracture Mechanics: Fundamentals and Applications*. 3rd Edition. Taylor & Francis.

14. Lide, D.R. (Ed.), 2000. *CRC Handbook of Chemistry and Physics*, 81st ed. CRC Press, Boca Raton (Florida), ISBN 0849304814.

15. De Meer, S., C.J. Spiers, and S. Nakashima. 2005. Structure and diffusive properties of fluid-filled grain boundaries: an in-situ study using infrared (micro) spectroscopy. *Earth Planet. Sci. Lett*. 232: 403–414.

16. Ibrahim, H., A. Ilinca, and J. Perron. 2008. Energy storage systems – characteristics and comparisons. Renewable and Sustainable Energy Reviews. 12:1221-1250.

17. Maleki, K. 2004. *Modélisation numérique du couplage entre l'endommagement et la perméabilité des roches – Application a l'étude des ouvrages de stockage souterrain*. PhD Thesis, Ecole Nationale des Ponts et Chaussées.